Electronic Supplementary Material (ESI) for ChemComm.
This journal is © The Royal Society of Chemistry 2020

Supporting Information

for

Mechanoresponsive Turn-On Phosphorescence by a Desymmetrization Approach

Yosuke Tani,* Mao Komura, and Takuji Ogawa*

Department of Chemistry, Graduate School of Science, Osaka University
Machikaneyama 1-1, Toyonaka, Osaka 560-0043, Japan
E-mail: y-tani@chem.sci.osaka-u.ac.jp; ogawa@chem.sci.osaka-u.ac.jp

Table of Contents

1. Instrumentation and Chemicals 2
2. Synthesis Procedures for **BrH** 3
3. Stimuli-Responsive Behavior of Diketones 5
4. Single Crystal X-ray Structure Analysis 9
5. Analysis Based on Photophysical Kinetic Constants 21
6. Conformation in the Amorphous 24
7. NMR Charts 28
8. References 32

1. Instrumentation and Chemicals

Unless otherwise noted, all the reactions were performed in a nitrogen atmosphere using anhydrous solvents and heat-gun-dried glassware on a dual-manifold Schlenk line. ^{1}H and $^{13}C\{^{1}H\}$ NMR spectra were recorded on a JEOL ECS400 spectrometer. Chemical shift values (δ) are reported in ppm and are calibrated to tetramethylsilane (0.00 ppm) or residual solvent (7.26 ppm in $CDCl_3$ or 2.05 ppm in $(CD_3)_2CO$) for ^{1}H, and to $CDCl_3$ (77.0 ppm) for ^{13}C NMR. Melting points were measured in a glass capillary with a Barnstead/Thermolyne Mel-Temp melting point apparatus. High-resolution mass spectra (ESI-HRMS) were obtained with a Thermo Fisher Scientific LTQ Orbitrap XL mass spectrometer. Elemental analysis (EA) was conducted on a Yanaco MT-5 or MT-6 recorder. All the photophysical properties (i.e., UV-vis absorption, photoluminescence (PL), and excitation spectra, PL quantum yields (PLQY), and PL lifetimes) were measured at room temperature (RT) under air unless otherwise noted. UV-vis absorption and PL spectra of solutions were obtained using a Shimadzu UV-3150 spectrometer and a JASCO FP-8200 spectrofluorometer, respectively. Solid-state PL spectra were obtained using a JASCO FP-8200 spectrofluorometer, a JASCO FP-6500N spectrofluorometer, or a HORIBA Fluorolog3-211 spectrometer. PLQYs of a cyclohexane solution of **BrH** and solids of **BrH**, **BrBr**, and **HH** were determined by the relative method using quinine sulfate as a standard[1] and by the absolute method using a JASCO FP-6500N spectrofluorometer, a Hamamatsu photonics C11347-01 spectrometer, or C9920-02 spectrometer with an integrating sphere, respectively. PL lifetime measurements for solids and a solution were performed using a JASCO FP-6500N spectrofluorometer or a HORIBA Fluorolog3-211 spectrometer. Analytical thin-layer chromatography (TLC) was performed on aluminum plates bearing a layer of Merck silica gel 60 F_{254}. Column chromatography was carried out on silica-gel 60 (Kanto Chemical Co., Inc., spherical, 63–210 μm).

Anhydrous THF and CH_2Cl_2 were purchased from Wako Chemical Co., Inc. and Kanto Chemical Co., Inc., respectively, and further purified by passage through activated alumina under positive nitrogen pressure as described by Grubbs et al.[2] Unless otherwise noted, chemicals obtained from commercial suppliers were used without further purification. 2-(Pentafluorophenyl)-6,7-dihydro-5*H*-pyrrolo[2,1-*c*][1,2,4]triazol-2-ium tetrafluoroborate (**S1**), 1,2-bis[3-bromo-5-(triisopropylsilyl)thiophen-2-yl]ethane-1,2-dione (**BrBr**) and 1,2-bis[5-(triisopropylsilyl)thiophen-2-yl]ethane-1,2-dione (**HH**) were synthesized according to the literature.[3]

2. Synthesis Procedures for BrH

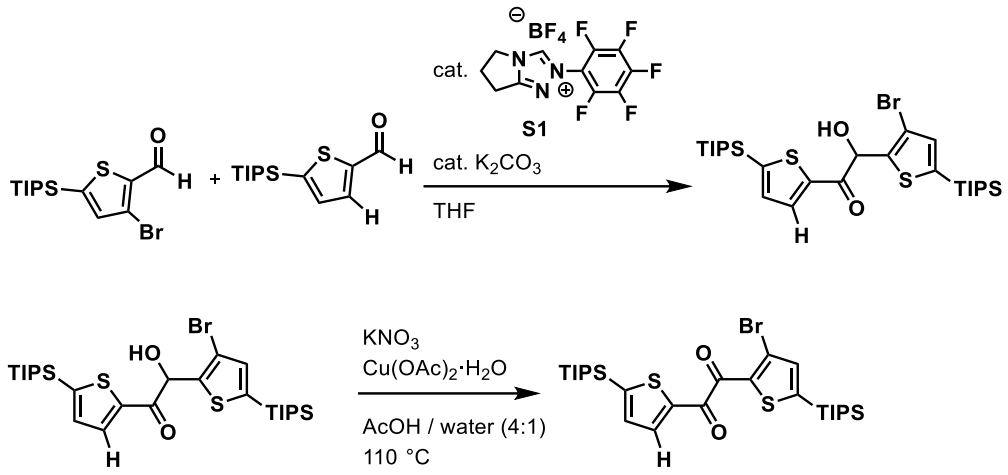

Scheme S1. Synthesis of BrH

1,2-bis[3-bromo-5-(triisopropylsilyl)thiophen-2-yl]-2-hydroxyethan-1-one (S2)

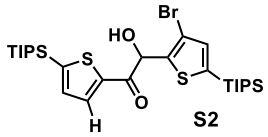

S2 was synthesized via cross-benzoin condensation with a modified procedure.[4] To a Schlenk tube were added K_2CO_3 (23 mg, 0.16 mmol) and triazolium salt **S1** (63 mg, 0.17 mmol), and the tube was shortly evacuated and backfilled with N_2 three times. THF (4 mL) was added via a syringe and the suspension stirred for 15 minutes. To the pale red suspension were added 2-formyl-5-(triisopropylsilyl)thiophene (2.69g, 10 mmol, 2.5 equiv.) and 3-bromo-2-formyl-5-(triisopropylsilyl)thiophene (1.50 g, 4.0 mmol, 1.0 equiv.) under a flow of N_2. The mixture was stirred for 72 h at RT, and then quenched by adding aq. NH_4Cl and CH_2Cl_2. The organic layer was separated and the aqueous layer was extracted with CH_2Cl_2. The combined organic extracts were dried over $MgSO_4$, filtered and then evaporated. The residue was purified by silica-gel column chromatography twice (eluent: hexane/CH_2Cl_2 2:1 for the first time and hexane/AcOEt 20:1 for the second time), and recrystallization from hexane for six times (until the complete disappearance of the homo-benzoins was confirmed by ^{1}H NMR) to give **S2** (0.68 g, 28%) as a white solid. **^{1}H NMR** (400 MHz, $CDCl_3$) δ: 7.78 (d, *J* = 3.7 Hz, 1H), 7.20 (d, *J* = 3.7 Hz, 1H), 7.08 (s, 1H), 6.08 (d, *J* = 5.5 Hz, 1H), 4.51 (d, *J* = 5.5 Hz, 1H), 1.32-1.25 (m, 6H), 1.07-1.00 (m, 36H). **^{13}C NMR** (100 MHz, $CDCl_3$) δ: 189.23, 147.76, 142.93, 141.29, 137.73, 137.58, 136.12, 134.29, 113.10, 71.04, 18.37, 18.35, 11.59, 11.59. **ESI-HRMS** (*m*/*z*): $[M+Na]^+$ calcd for $C_{28}H_{45}O_2BrS_2Si_2Na$, 637.1637; found, 637.1631. The structure with the carbonyl group on the 5-triisopropylsilylthienyl ring can be distinguished from its

isomer by the presence of a doublet peak at 7.78 ppm, which is assigned to the hydrogen *ortho* to the carbonyl group. This is further confirmed by comparing the ^{1}H NMR spectra with the reported data for the corresponding thenoins with or without bromo group.[3]

1-[3-bromo-5-(triisopropylsilyl)thiophen-2-yl]-2-[5-(triisopropylsilyl)thiophen-2-yl]ethane-1,2-dione (BrH)

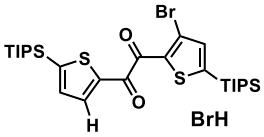

To a Schlenk tube were added **S2** (394 mg, 0.64 mmol), KNO_3 (89 mg, 0.88 mmol), $Cu(OAc)_2{\cdot}H_2O$ (1.8 mg, 9 μmol), and AcOH/H_2O (4:1, 3.0 mL). The mixture was stirred overnight at 110 °C. After cooling to RT, the mixture was quenched by adding H_2O and CH_2Cl_2. The organic layer was separated and the aqueous layer was extracted with CH_2Cl_2 three times. The combined organic extracts were dried over $MgSO_4$, filtered and then evaporated. The residue was purified by recrystallization from a stirred solution in $CHCl_3$ by adding methanol at RT to give pure **BrH** (294 mg, 74%) as a slightly yellow powder. **m.p.** 90–91 °C. **^{1}H NMR** (400 MHz, $(CD_3)_2CO$) δ: 8.11 (d, *J* = 3.9 Hz, 1H), 7.53 (d, *J* = 3.9 Hz, 1H), 7.48 (s, 1H), 1.48–1.44 (m, 6H), 1.15 (d, *J* = 7.3 Hz, 36H). **^{13}C NMR** (100 MHz, $CDCl_3$) δ: 182.22, 181.89, 150.55, 149.09, 142.73, 140.41, 137.31, 136.45, 134.77 120.16, 18.48, 18.43, 11.70, 11.58. **EA** Calcd for $C_{28}H_{45}BrO_2S_2Si_2$: C, 54.79; H, 7.39. Found: C, 54.76; H, 7.41. Single crystal of **1** (CCDC-1986447–1986451) was obtained by slow cooling of hot hexane solution to 9 °C.

3. Stimuli-Responsive Behavior of Diketones

Typical procedure for preparation of the solid samples

To a stirred solution of **BrH** (465.8 mg) in $CHCl_3$ (3.8 mL) at 0 °C was added dropwise MeOH until the solid started to precipitate (11.38 mL). After the addition, stirring was stopped and the mixture was left for 20 min at 0 °C. The precipitates were collected by vacuum filtration and washed with cold MeOH to give pristine (crystalline) **BrH**. Ground powder was prepared by uniformly grinding the pristine **BrH** for 20 min with an agate mortar and pestle.

PL spectra of the solid diketones

The PL spectra for pristine and ground **BrH** and **BrBr** (Figure 2 in the main text) were measured with the excitation wavelength (λ_{ex}) of 380 nm, using a JASCO FP-8200 spectrofluorometer with a L42 sharp cut filter (HOYA, long pass, >420 nm) and a U340 band pass filter (HOYA). The PL spectrum of pristine **HH** was measured with a HORIBA Fluorolog3-211 spectrometer (λ_{ex} = 400 nm, Figure S1).

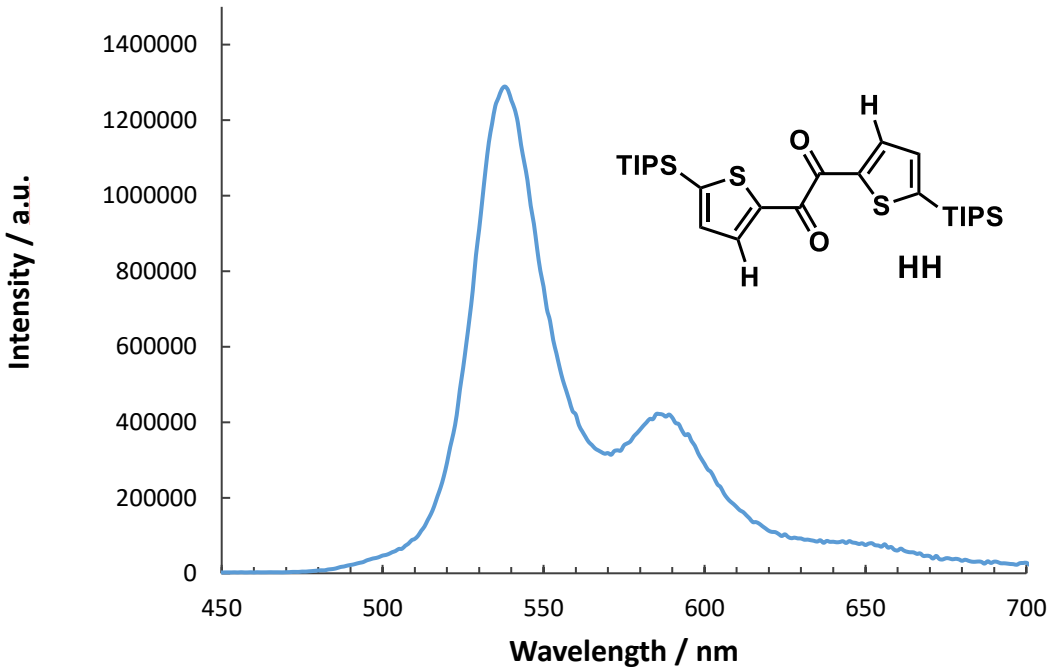

Figure S1. PL spectra of pristine **HH** (λ_{ex} = 400 nm). Inset shows the chemical structure of **HH**.

PLQY of the solid diketones

PLQY was determined at RT with a Hamamatsu photonics C11347-01 or C9920-02 spectrometer with an integrating sphere (λ_{ex} = 370 nm for ground **BrH**, 370 nm for pristine and ground **BrBr**, and 400 nm for pristine **HH**). We were unable to determine the PLQY of pristine **BrH** because no emission was detected at all using the integrating sphere equipped on the C11347-01 spectrometer (Figure S2).

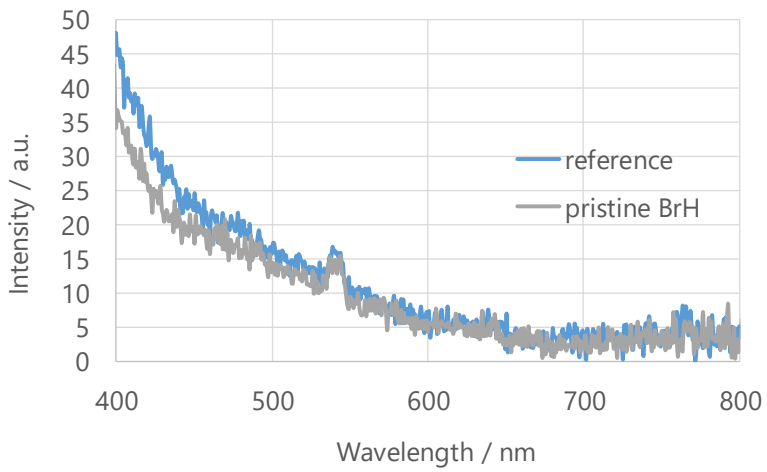

Figure S2. PL spectrum of pristine **BrH** measured using an integrating sphere (λ_{ex} = 320 nm).

Estimation of the turn-on ratio

To estimate the turn-on ratio (the ratio of the intensity before and after mechanical stimulation), the PL spectra of **BrH** in Figure 2 were measured as following using a JASCO FP-8200 spectrofluorometer. First, the pristine powder was placed between two 20 × 20 × 1 mm quartz plates using another 10 × 10 × 1 mm plate as a spacer and the PL spectrum was recorded. Next, the small plate was removed and the two larger plates were carefully rubbed together so that the loss of the powder is minimized, then the PL spectrum for the ground powder was measured. The turn-on ratio is estimated to be 276 as the ratio of intensities at the emission maxima (559 nm). In the PL spectrum of the pristine powder, the shoulder at approx. 530 nm may originate from the emission from crystalline domain while the other peaks from amorphous domain.

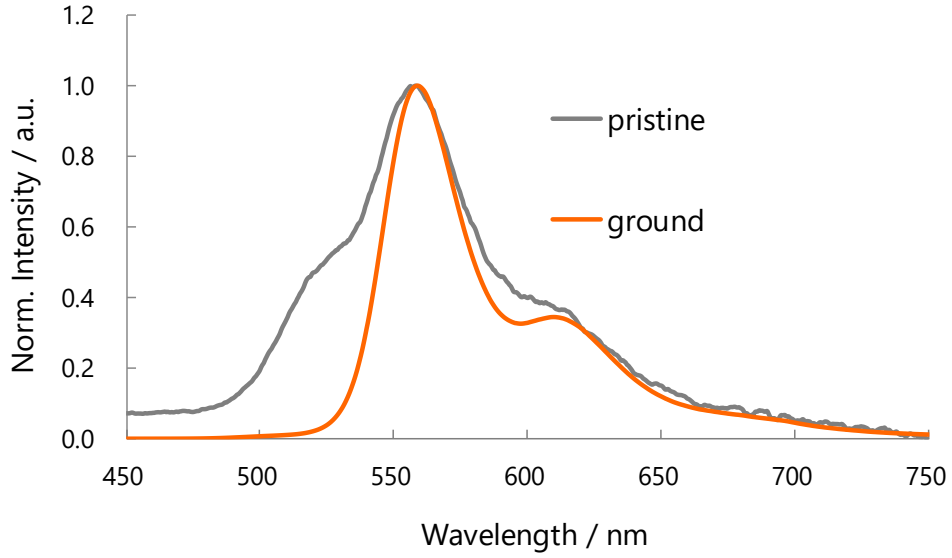

Figure S3. Normalized PL spectra of pristine (gray) and ground **BrH** (orange) at RT under air (λ_{ex} = 380 nm).

PL lifetimes in the solid-state

The PL decay curve of ground **BrH** was measured with a HORIBA Fluorolog3-211 spectrometer (Figure S4). The lifetime τ_p was obtained from a single-exponential fit using the igor software. The PL intensities of **BrH** was recorded at 560 nm (λ_{ex} = 370 nm).

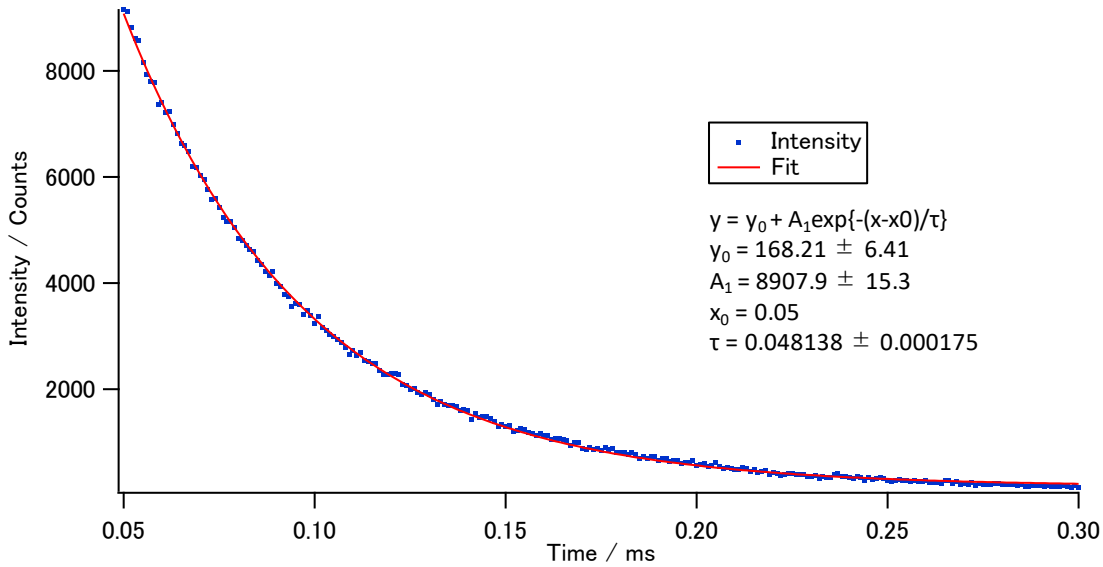

Figure S4. PL decay curve of ground **BrH** at RT under air. The red line denotes the fit to the curve. The PL intensity at 560 nm was recorded (λ_{ex} = 370 nm).

Photographs

Photographs in Figure 2 were taken using SONY NEX-5N under incandescent light or under irradiation with UV light (365 nm).

Powder X-ray diffraction

Powder X-ray diffraction (PXRD) patterns were collected on a PANalytical XPert PRO with CuKα radiation (λ = 1.5418 Å) (Figure S5).

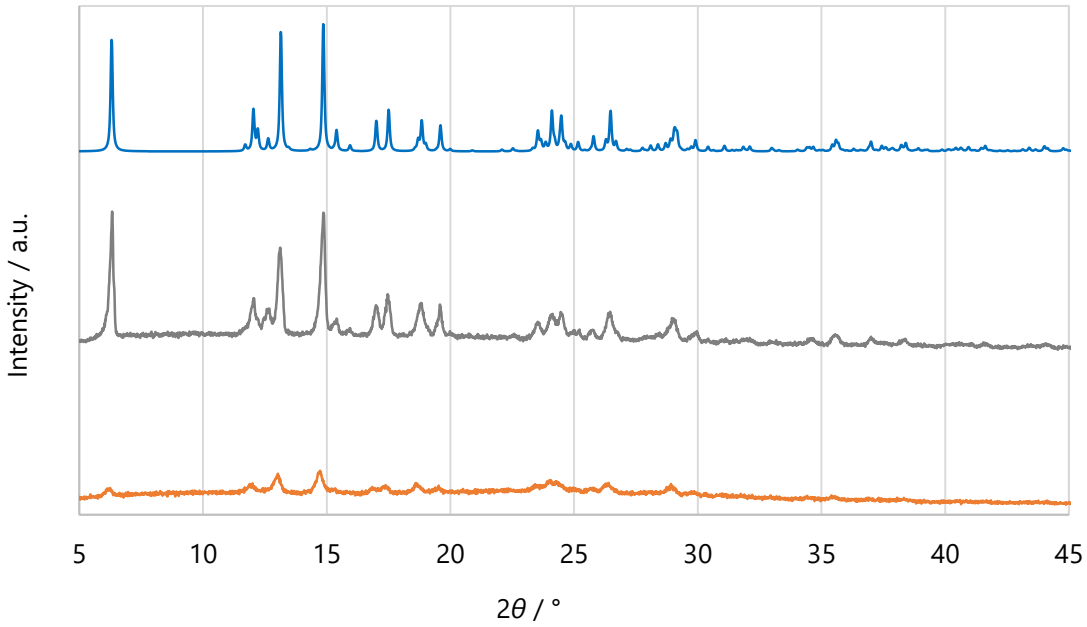

Figure S5. PXRD profiles of (from top to bottom) single crystal (simulated from the diffraction data recorded at RT), pristine, and ground solid of **BrH**.

4. Single Crystal X-ray Structure Analysis

Data were collected on a Rigaku XtaLab P200 diffractometer with graphite monochromated MoKα radiation (λ = 0.71075 Å) in the ω-scan mode. The crystals were cooled by a stream of cold N_2 gas. Collection, indexing, peak integration, cell refinement, and scaling of the diffraction data were performed using the CrystalClear software (Rigaku). The structures were solved by direct methods (SIR97) and refined by full-matrix least-square refinement on F^2 (SHELXL2014). The non-hydrogen atoms were refined anisotropically. All hydrogen atoms were placed on the calculated positions and refined using the riding model.

The ratio of the directional disorder in the **BrH** crystal is approx. 2:1 based on the refined site occupancy factors of the Br atoms (Table S1). A completely random (1:1) orientation would give the centrosymmetric *C*2/*c* space group, which is the same as that of **BrBr** crystal. However, in this case, the R1 factor increased from 3.56% to 9.15% for the diffraction data measured at 123 K, supporting that *Cc* space group is more appropriate for the **BrH** crystal and the ratio is not 1:1.

Table S1. Refined Site Occupancy Factors in the **BrH** Crystal

Temperature / K	Refined site occupancy factor	
	Br1	Br2
123	0.672(2)	0.328(2)
173	0.677(3)	0.323(3)
223	0.663(3)	0.337(3)
273	0.665(4)	0.335(4)
300	0.665(5)	0.335(5)

Table S2. Crystallographic Data for **BrH** (CCDC-1986447–1986451)

Empirical formula	$C_{28}H_{45}BrO_2S_2Si_2$	$C_{28}H_{45}BrO_2S_2Si_2$	$C_{28}H_{45}BrO_2S_2Si_2$	$C_{28}H_{45}BrO_2S_2Si_2$	$C_{28}H_{45}BrO_2S_2Si_2$
FW	613.85	613.85	613.85	613.85	613.85
T / K	123(2)	173(2)	223(2)	273(2)	300(2)
Crystal system	Monoclinic	Monoclinic	Monoclinic	Monoclinic	Monoclinic
Space group	*Cc*	*Cc*	*Cc*	*Cc*	*Cc*
a / Å	12.2344(17)	12.2742(19)	12.3126(17)	12.339(3)	12.362(3)
b / Å	9.4516(14)	9.4757(14)	9.5050(12)	9.5268(19)	9.5472(18)
c / Å	27.594(4)	27.688(4)	27.815(4)	27.927(6)	28.028(5)
α / °	90	90	90	90	90
β / °	91.677(3)	92.029(4)	92.260(3)	92.563(5)	92.689(5)
γ / °	90	90	90	90	90
V / Å^3	3189.5(8)	3218.3(8)	3252.7(8)	3279.6(12)	3304.3(12)
Z	4	4	4	4	4
D (calcd) / g·cm^{-3}	1.278	1.267	1.254	1.243	1.234
Crystal size / mm^3	0.27 × 0.20 × 0.10	0.27 × 0.20 × 0.10	0.27 × 0.20 × 0.10	0.27 × 0.20 × 0.10	0.27 × 0.20 × 0.10
Completeness	99.80%	95.10%	99.70%	99.60%	99.10%
GOF on *F2*	1.042	1.025	1.024	1.041	1.026
R1 [I > 2s (I)]	0.0356	0.0382	0.0447	0.0602	0.0614
wR2 (all data)	0.0861	0.0951	0.1184	0.1569	0.1634
CCDC number	1986447	1986448	1986449	1986450	1986451

Table S3. Crystallographic Data for **BrBr** (CCDC-1986442–1986446)

Empirical formula	$C_{28}H_{44}Br_2O_2S_2Si_2$	$C_{28}H_{44}Br_2O_2S_2Si_2$	$C_{28}H_{44}Br_2O_2S_2Si_2$	$C_{28}H_{44}Br_2O_2S_2Si_2$	$C_{28}H_{44}Br_2O_2S_2Si_2$
FW	692.75	692.75	692.75	692.75	692.75
T / K	123(2)	173(2)	223(2)	273(2)	300(2)
Crystal system	Monoclinic	Monoclinic	Monoclinic	Monoclinic	Monoclinic
Space group	*C* 2/*c*	*C* 2/c	*C* 2/*c*	*C* 2/*c*	*C* 2/*c*
a / Å	12.1566(14)	12.2000(17)	12.2294(16)	12.2570(16)	12.2729(19)
b / Å	9.5772(11)	9.5964(12)	9.6130(12)	9.6358(13)	9.6494(15)
c / Å	28.031(3)	28.151(4)	28.292(4)	28.442(4)	28.534(5)
α / °	90	90	90	90	90
β / °	92.526(3)	92.890(4)	93.195(3)	93.474(3)	93.614(4)
γ / °	90	90	90	90	90
V / $Å^3$	3260.4(6)	3291.6(8)	3320.9(8)	3353.0(8)	3372.5(9)
Z	4	4	4	4	4
D (calcd) / $g \cdot cm^{-3}$	1.411	1.398	1.386	1.372	1.364
Crystal size / mm^3	0.20 × 0.15 × 0.06	0.20 × 0.15 × 0.06	0.20 × 0.15 × 0.06	0.20 × 0.15 × 0.06	0.20 × 0.15 × 0.06
Completeness	99.60%	99.20%	98.80%	99.10%	99.30%
GOF on *F2*	1.038	1.038	1.012	1.032	1.032
R1 [*I* > 2s (*I*)]	0.046	0.0475	0.0516	0.0561	0.0605
wR2 (all data)	0.1086	0.1223	0.1311	0.1569	0.1705
CCDC number	1986442	1986443	1986444	1986445	1986446

Numerical evaluation of the isostructurality

The unit-cell similarity index (Π), which is a descriptor of the degree of isostructurality, was calculated to be 0.006 for the structures of **BrH** and **BrBr** at 123 K according to the following equation:

$$\Pi = \frac{a+b+c}{a'+b'+c'} - 1$$

where a, b, c and a', b', c' are the orthogonalized lattice parameters ($a + b + c > a' + b' + c'$). A Π value close to zero (≤0.01) indicates a high degree of isostructurality for the two crystals.

As another isostructurality descriptor, the root mean square deviation of the molecular coordinates (termed as the molecular isometricity index) was calculated (Table S4). These values are quite small, indicating the molecular conformational similarity between **BrBr** and **BrH** in the crystals. For comparison, the value for **BrBr** and **HH** was calculated, which are much larger than those for **BrBr** and **BrH**. The crystal structure of **HH** has been reported previously (CCDC-1906441).[3]

Table S4. Root Mean Square Deviation (Å) of the Molecular Coordinates

	4 atoms[a]	14 atoms[b]	34 atoms[c]
BrBr & **BrH**	0.056	0.100	0.117
BrBr & **HH**	0.215	0.554	—

[a] The dicarbonyl moiety (O–C–C–O). [b] The thienyl diketone core (i.e., without the silyl groups, H, and Br). [c] All atoms except H and Br.

Evaluation of the interaction energy in the crystals

In the crystal, one molecule of **BrBr** possesses 16 adjacent molecules including 7 independent pairs (Figure S6). Among them, short-contact (distance between two atoms below the sum of their van der Waals radii) is found only in the pair with green. The interaction energies (E_{int}) for those 7 independent pairs were evaluated through density functional theory (DFT) calculations at the B3LYP-D3/6-311G(d) level with the basis set superposition error correction implemented using the counterpoise method (Table S5).[5] All the calculations were carried out using Gaussian 16 program packages.[6] All the geometries were taken from the crystal structure at 123 K (CCDC-1906440).

Due to the non-centrosymmetric structure and the disorder in the **BrH** crystal, the short-contact pair (the pair with green) in **BrBr** corresponds to the eight pairs in the **BrH** crystal (Figure S7). E_{int} for those pairs were evaluated using the crystal structure at 123 K (CCDC-1986447) in the same manner (Table S4): –14.53 to –15.76 kcal/mol for the pairs with the void between them (A, B, A', and B') while –15.31 to –17.04 kcal/mol for those without void (C, D, C', and D'). The decrease of E_{int} suggests that the void loosens the crystal packing of **BrH**. Correspondingly, the melting point of pristine **BrH** was substantially lower (90–91 °C) than that of **BrBr** (157–160 °C).

Table S5. Interaction energy in the **BrBr** and **BrH** crystals

Pair with	Interaction energy / kcal mol^{-1}	Pair	Interaction energy / kcal mol^{-1}
Green	–18.03	A	–14.96
Violet	–7.05	B	–14.53
Magenta	–5.30	C	–17.04
Red	–5.19	D	–16.30
Light blue	–2.20	A'	–15.76
Light green	–1.43	B'	–15.32
Blue	–1.31	C'	–16.01
		D'	–15.31

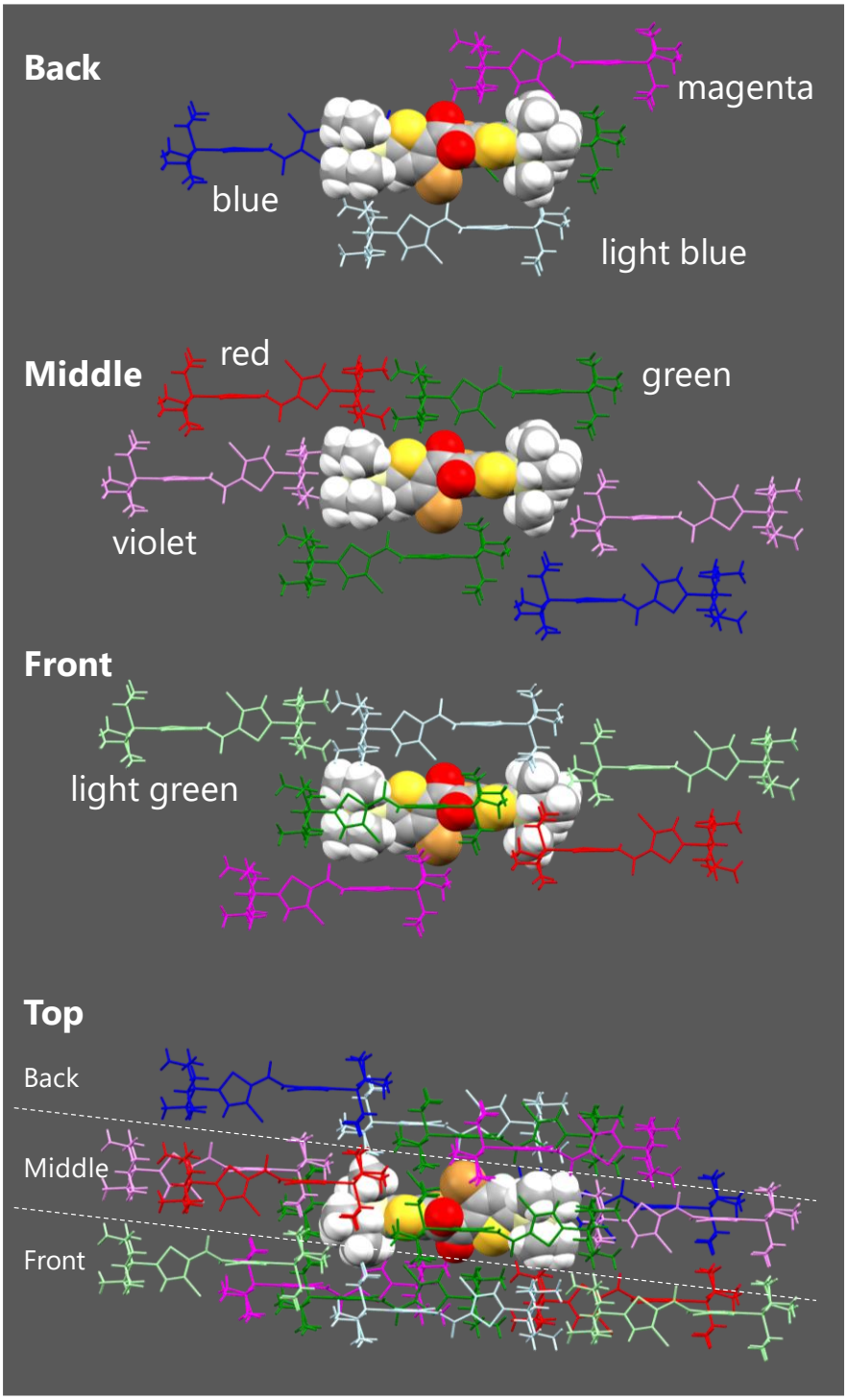

Figure S6. Seven independent pairs (green, violet, magenta, red, light blue, light green, and blue) with the central molecule (depicted as space-filling model).

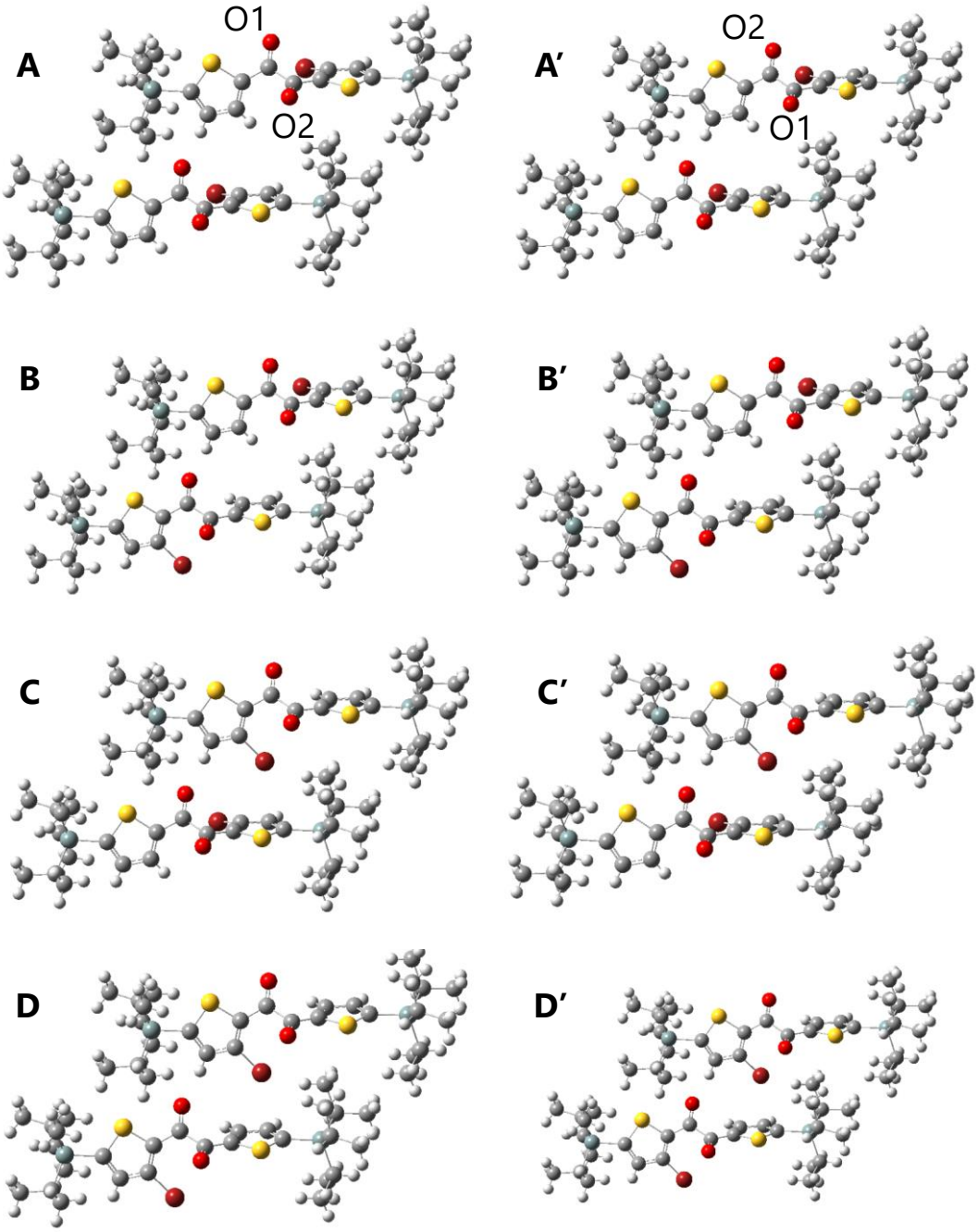

Figure S7. Input structures for the calculation of E_{int} for **BrH**.

ORTEP structures of BrH and BrBr at different temperatures

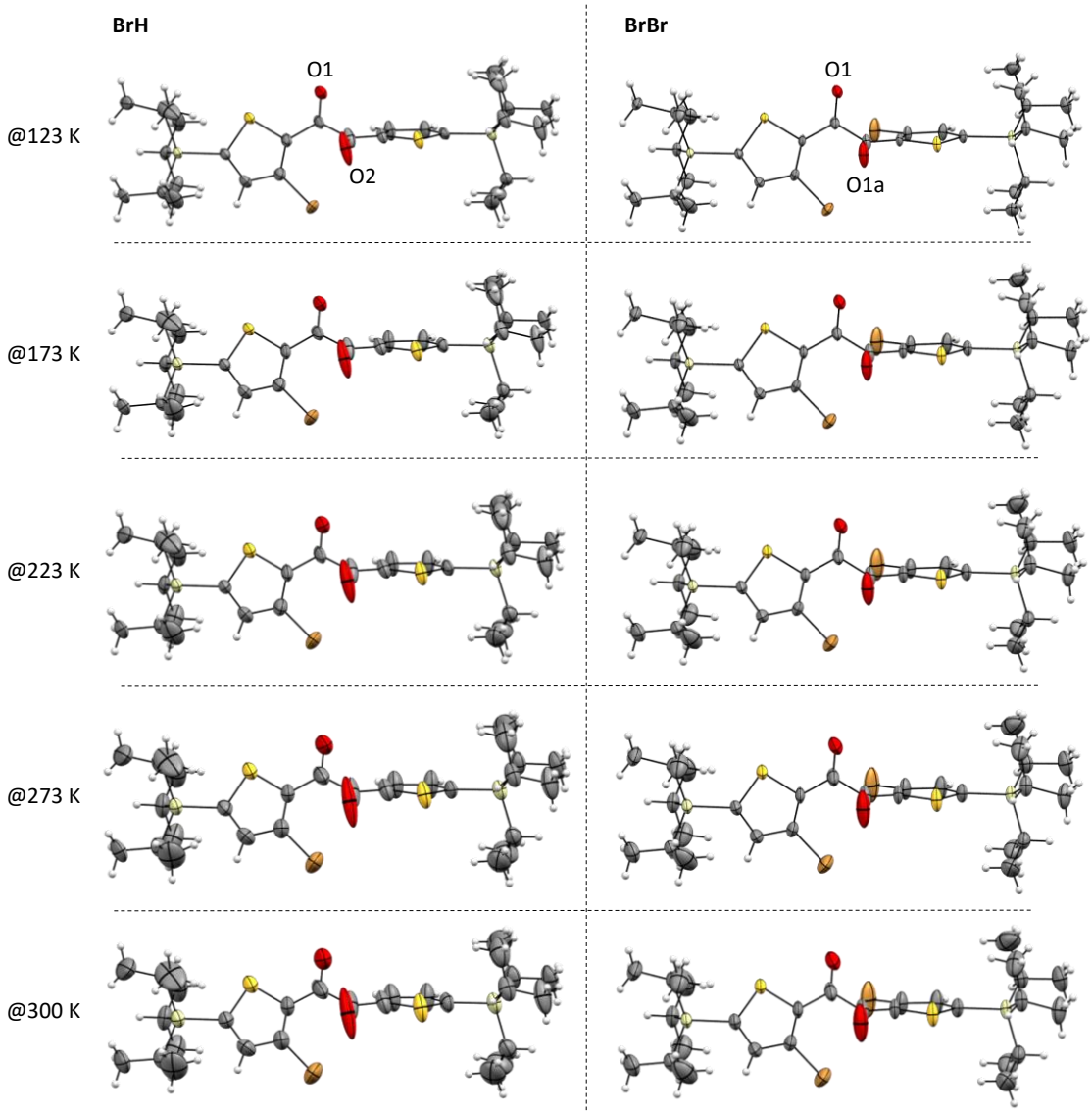

Figure S8. ORTEP structures of **BrH** (left) and **BrBr** (right) at different temperatures. The thermal ellipsoids are set at the 50% probability level.

Temperature-dependence of the anisotropic displacement parameters

The anisotropic atomic displacement parameter (ADP) represents probability density functions of atomic position from the mean position. The three eigenvalues (λ_1–λ_3) of an ADP matrix are proportional to the length of three principal axes of the corresponding thermal ellipsoid in ORTEP model. It should be noted that λ represents not only dynamic atomic motion but also static displacive disorder. Therefore, we investigated its temperature dependence to distinguish the dynamic (thermal) motion of atoms from static contribution associated with the substitutional disorder of Br atoms. For harmonic thermal motion in the classical regime, λ is expected to correlate linearly with temperature (T) and reach 0 at T = 0 K. Thus, the slope represents a contribution from dynamic disorder, i.e., thermal motion of the atom, while the intercept represents a contribution from static disorder, which, in this case, associate with the disorder regarding molecular direction.

Specifically, λ_1–λ_3 for selected atoms (labeled in Figure S9) were calculated from corresponding ADP matrices, which were obtained through single-crystal X-ray structure analyses at five different temperatures (123, 173, 223, 273, and 300 K), and then plotted against temperature (Figures S10–S12 and Table S6). The intercepts of λ_1–λ_3 for the oxygen atoms were close to zero ($\leq$ 0.010 Å^2) except λ_1 for O1 in **BrH**, which is 0.060 Å^2, indicating that the prolate shape of the thermal ellipsoid for O1 contains contribution from the static disorder while those of others do not. The largest eigenvalue, λ_1, for O1 and O2 in **BrH** and that for O1 in **BrBr** have slopes of 7.7×10^4, 1.4×10^5, and 7.3×10^4 Å^2/K, respectively, demonstrating that the thermal motion of O2 in **BrH** is considerably larger than that of **BrBr**.

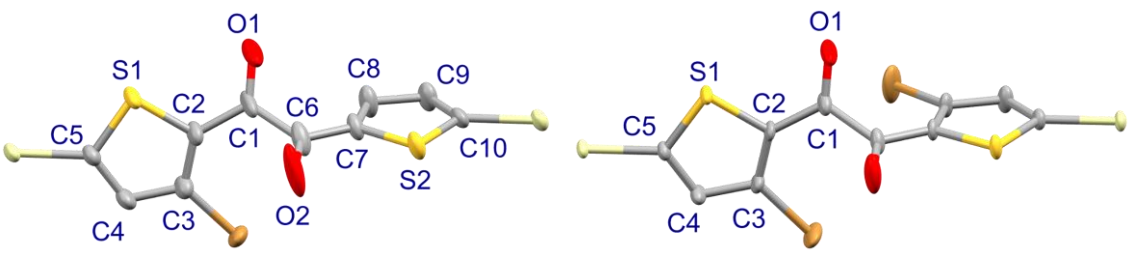

Figure S9. Atom labeling for **BrH** (left) and **BrBr** (right).

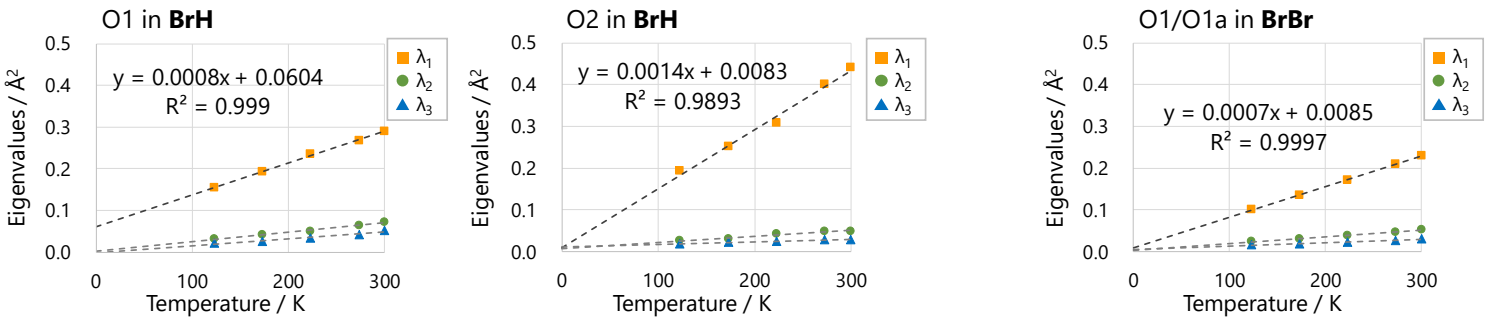

Figure S10. Temperature dependence of λ_1–λ_3. Inset: linear fitting functions for λ_1.

Table S6. Eigenvalues of O1/O2 and their Slopes and Intercepts against Temperature

	BrH						**BrBr**		
	O1			O2			O1		
T / K	λ_1 / Å^2	λ_2 / Å^2	λ_3 / Å^2	λ_1 / Å^2	λ_2 / Å^2	λ_3 / Å^2	λ_1 / Å^2	λ_2 / Å^2	λ_3 / Å^2
123	0.154	0.031	0.021	0.192	0.025	0.018	0.100	0.023	0.016
173	0.193	0.041	0.026	0.251	0.030	0.021	0.134	0.030	0.019
223	0.234	0.050	0.034	0.308	0.041	0.024	0.171	0.038	0.023
273	0.268	0.063	0.042	0.401	0.048	0.029	0.208	0.047	0.026
300	0.290	0.072	0.052	0.441	0.049	0.028	0.229	0.052	0.031
Slope / Å^{2}K^{-1}	7.7.E-04	2.3.E-04	1.7.E-04	1.4.E-03	1.6.E-04	6.9.E-05	7.3.E-04	1.6.E-04	8.3.E-05
Intercept / Å^2	6.0.E-02	2.1.E-03	-2.1.E-03	8.3.E-03	6.7.E-03	1.0.E-02	8.5.E-03	2.7.E-03	4.7.E-03
R^2	0.999	0.989	0.958	0.989	0.971	0.975	1.000	0.999	0.972

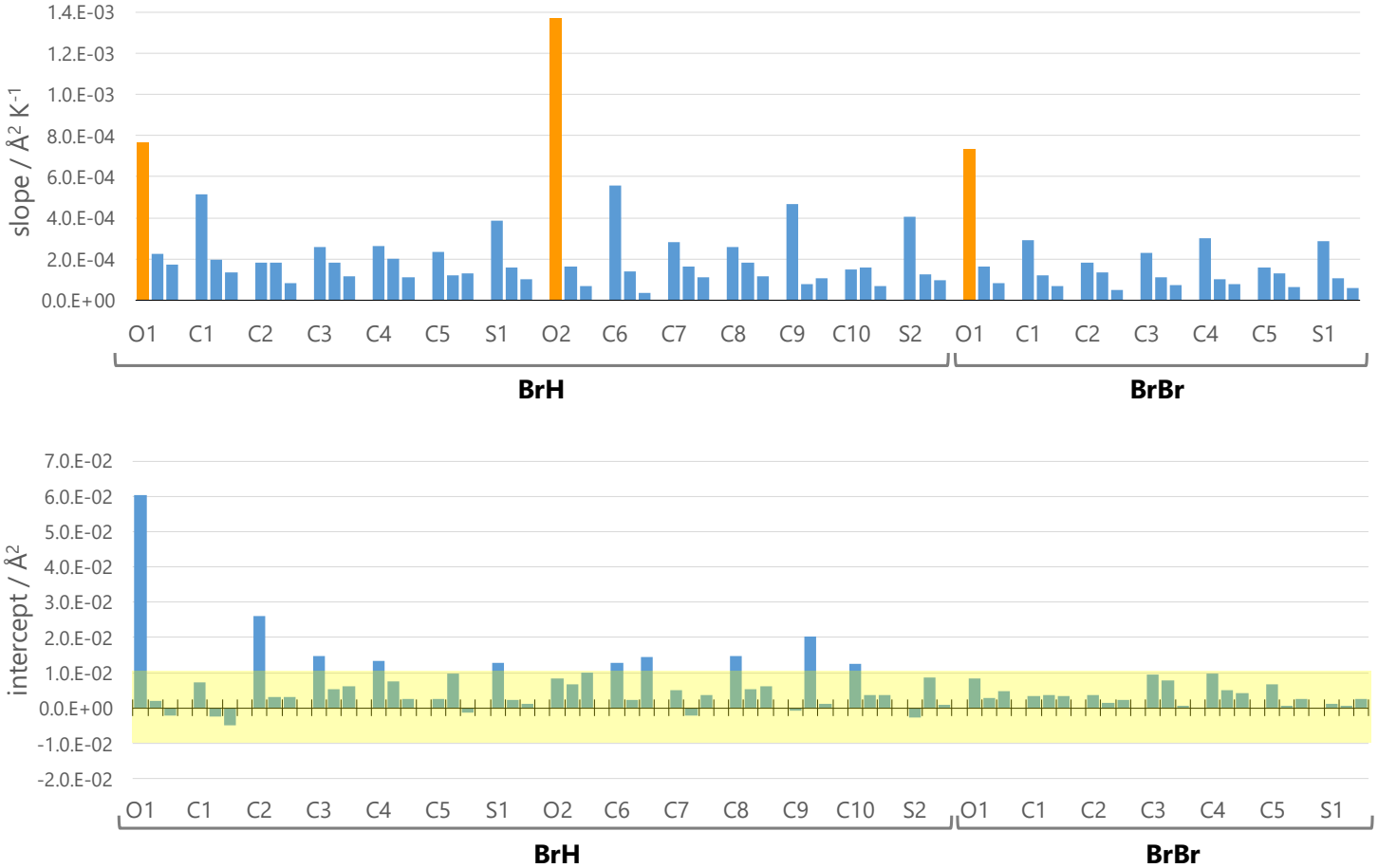

Figure S11. Slopes (top) and intercepts (bottom) for core atoms of **BrH** and **BrBr**. Three bars of each sections represent λ_1–λ_3 (from left to right). The slopes of λ_1 for O1/O2 are significantly large, implying the thermal motion in the crystal. Large intercepts are found in O1, C2, and C9 in **BrH** while those of the other atoms in **BrH** and all the atoms in **BrBr** are close to zero (≤0.01, highlighted in yellow).

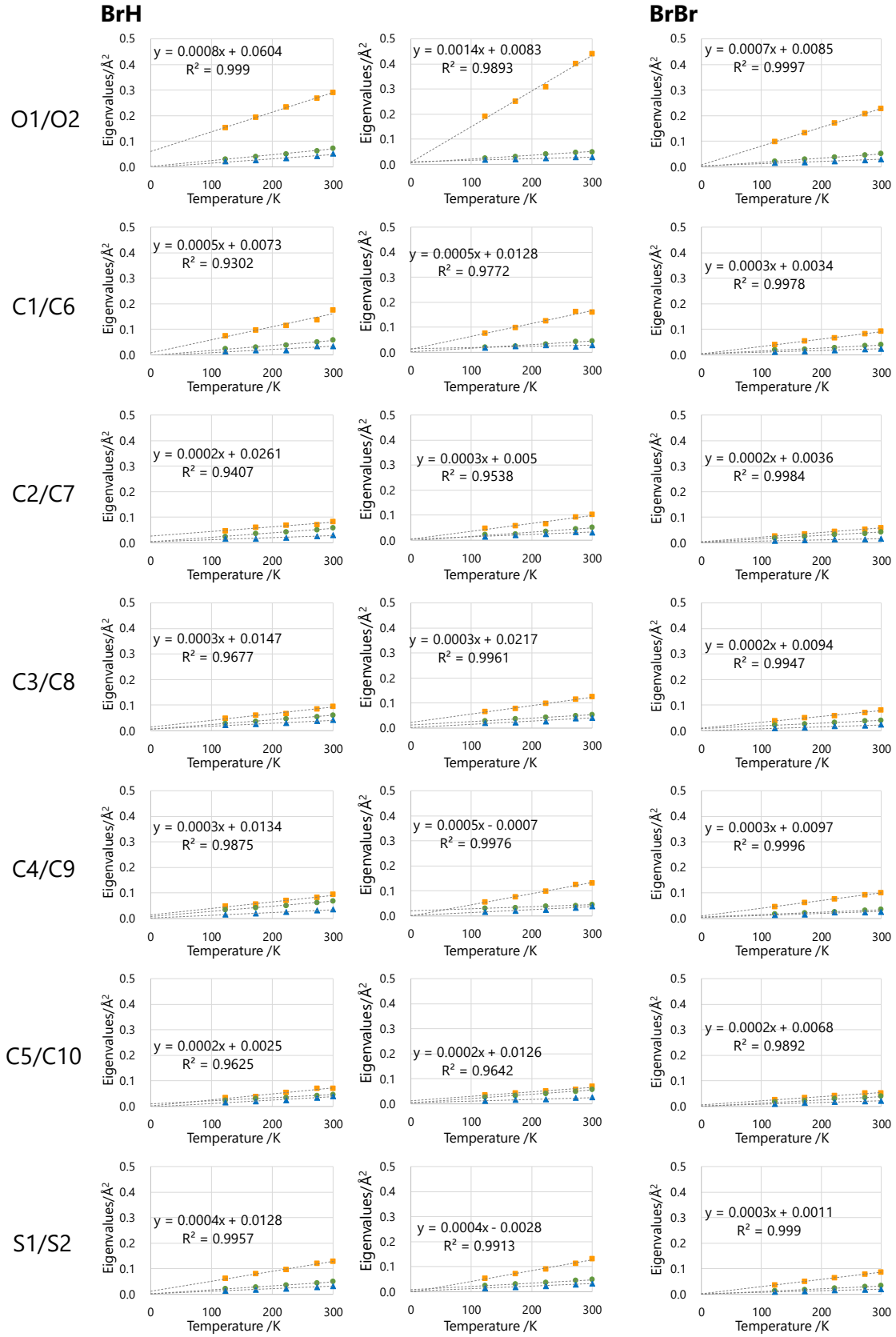

Figure S12. λ–T plots for the selected atoms in **BrH** and **BrBr**.

5. Analysis Based on Photophysical Kinetic Constants

In principle, phosphorescence quantum yield Φ_p can be expressed as follows:

$$\Phi_p = \Phi_{ISC}\frac{k_p}{k_p + k_{nr}} = \Phi_{ISC}k_p\tau_p \quad \text{(S1)}$$

where k_p and k_{nr} is the rate constants of phosphorescence and nonradiative decay from T1, respectively, Φ_{ISC} is the quantum efficiency of intersystem crossing, and τ_p is the phosphorescence lifetime. From eq S1 it is clear that Φ_p become small when k_p become small and/or k_{nr} become large. The contribution from k_p and k_{nr} on Φ_p can be distinguished through the experimental measurement of τ_p. Therefore, we can know the controlling factor of phosphorescence quenching as either relative decrease in k_p or relative increase in k_{nr}, through the analysis based on the kinetic constants. We regard Φ_{ISC} as unity because no discernible fluorescence emission was observed for both diketones.

At 77 K, the phosphorescence decay rate constant k_p of **BrH** was on the same order as that of **BrBr** (230 and 310 s^{-1}, respectively), indicating that electronically unfavorable factors, including heavy atom effect, are not very pronounced. Thus, such factors can be excluded as the principle reason for the nonemissive nature of the **BrH** crystal (Table 1).

PLQY of pristine diketones at 77 K

PLQY was determined to be 66% for pristine **BrH** and 84% for pristine **BrBr** using a JASCO FP-6500N spectrometer with an integrating sphere at 77 K (λ_{ex} = 400 nm for both **BrH** and **BrBr**).

Low-temperature PL spectra of pristine diketones

PL spectra of pristine **BrH** (Figure S13) and **BrBr** (Figure S14, blue line) were measured at 77 K (λ_{ex} = 400 nm) using a JASCO FP-6500N spectrometer with a L42 sharp cut filter (HOYA, long pass, >420 nm). For comparison, the one for **BrBr** at RT was obtained using a JASCO FP-8200 spectrometer with the L42 sharp cut filter and a U340 band pass filter (HOYA) (Figure S14, red line).

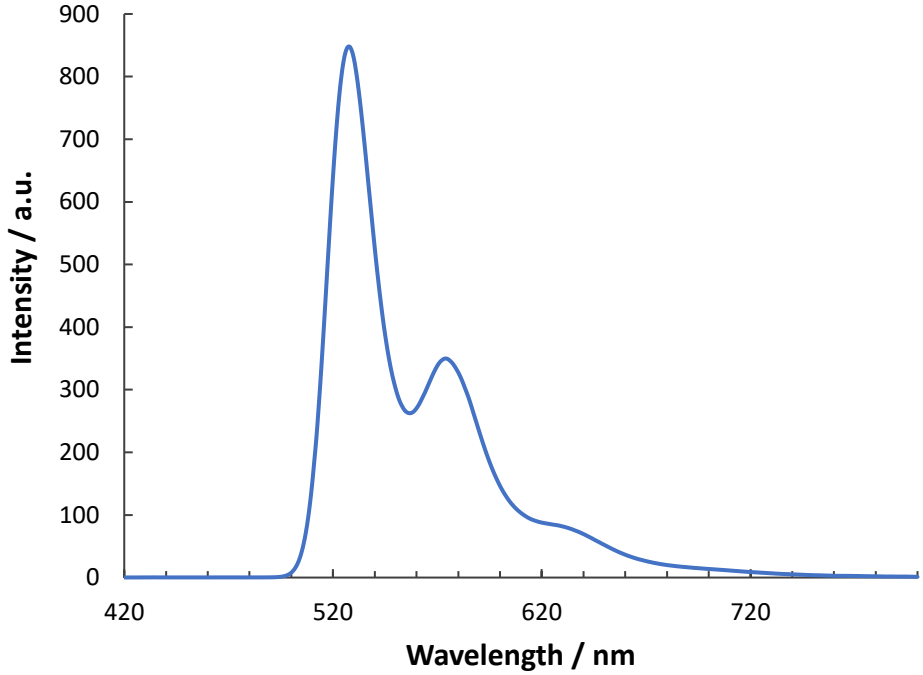

Figure S13. Steady state PL spectra of pristine **BrH** at 77 K (λ_{ex} = 400 nm).

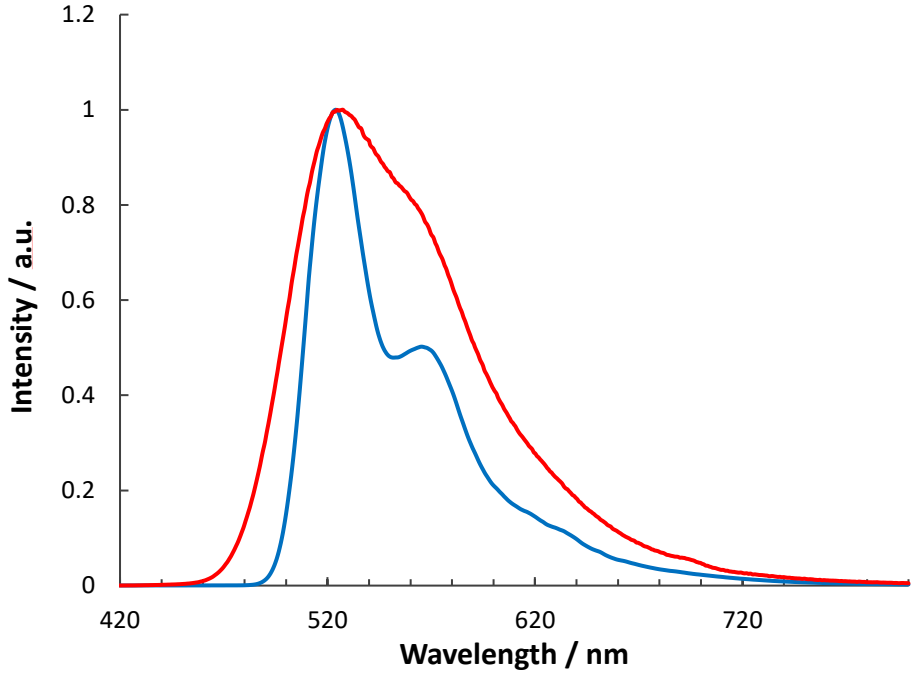

Figure S14. Steady state normalized PL spectra of pristine **BrBr** (red, RT, λ_{ex} = 360 nm, blue, 77K; λ_{ex} = 400 nm).

Phosphorescence lifetimes of pristine diketones at 77 K

PL decay curves of pristine **BrH** and **BrBr** were measured with a JASCO FP-6500N spectrofluorometer at 77 K (Figures S15 and S16, respectively). τ_p was obtained from a single-exponential fit using the igor software. The PL intensities at 528 nm for **BrH** and 524 nm for **BrBr** were recorded (λ_{ex} = 400 nm for both).

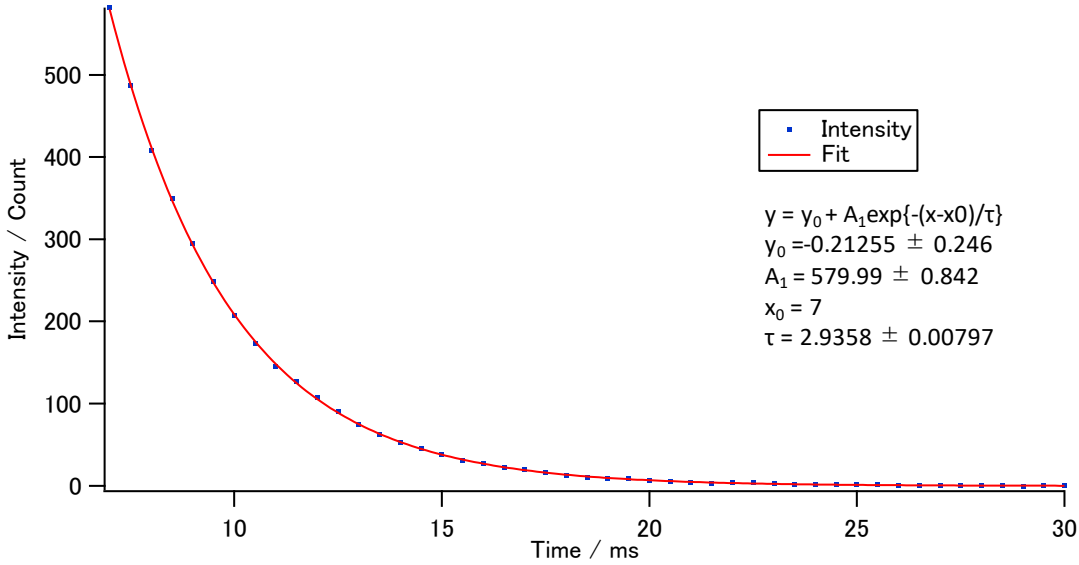

Figure S15. PL decay curve of pristine **BrH** at 77K. The red line denotes the fit to the curve. The PL intensity at 528 nm was recorded (λ_{ex} = 400 nm).

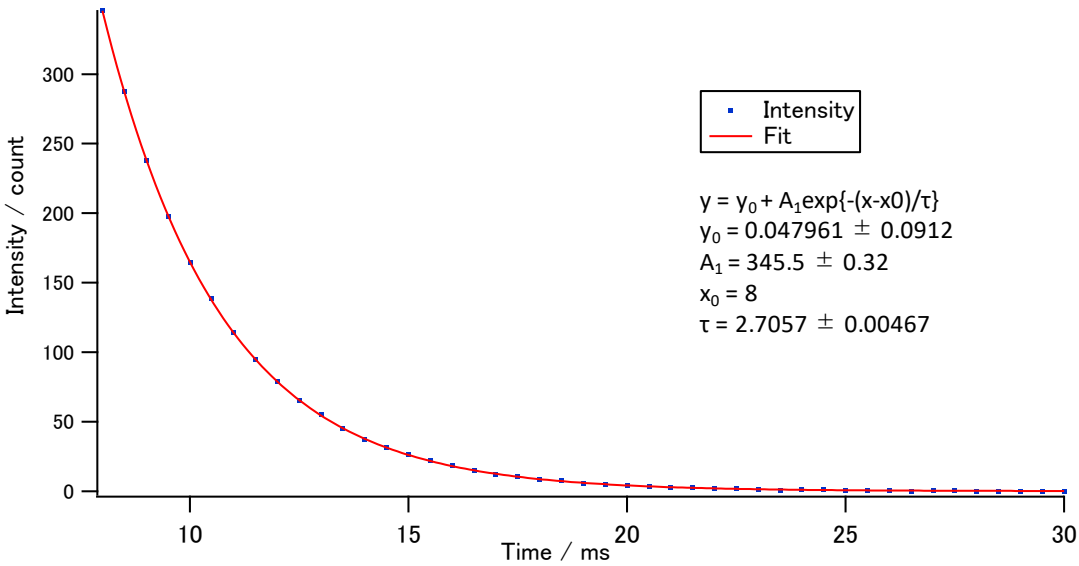

Figure S16. PL decay curve of pristine **BrBr** at 77K. The red line denotes the fit to the curve. The PL intensity at 524 nm was recorded (λ_{ex} = 400 nm).

6. Conformation in the Amorphous

Absorption and excitation spectra of ground BrH

We measured the diffuse reflectance spectrum of ground **BrH** mixed with $BaSO_4$ using a SHIMADZU UV-3150 spectrometer equipped with a SHIMADZU ISR-3100 integrating sphere attachment. Kubelka-Munk conversion of the spectrum gave the solid-state absorption spectrum (Figure S17 top, gray). Excitation spectrum of the ground **BrH** powder were measured using a JASCO FP-8200 spectrometer (Figure S17 top, orange). For comparison, UV-vis absorption spectrum of **BrH** in spectral grade cyclohexane (2.0×10^{-5} M) was measured using a Shimadzu UV-3150 spectrometer (Figure S17 top, blue).

The absorption spectrum of the ground **BrH** almost overlapped that of **BrH** solution, while the excitation spectrum was totally different from them, with a maximum at 375 nm. To assign these peaks, (time-dependent, TD) DFT calculation was conducted at the B3LYP-D3/6-311G(d) level of theory using Gaussian 16 program packages.[6] First, the geometry of the skew and planar conformers of **BrH** were optimized and none of them had imaginary frequencies (Figure S18). Next, single-point TD-DFT calculation of the optimized structures was performed to obtain oscillator strengths of the excitations, and then the absorption spectra of both conformers were simulated (Figure S17 bottom, blue and orange for the skew and planar conformers, respectively). The comparison of the experimental spectra with the simulated ones suggested that the major conformer in the ground **BrH** is the skew, whereas the RTP emission comes from the minor planar conformer.

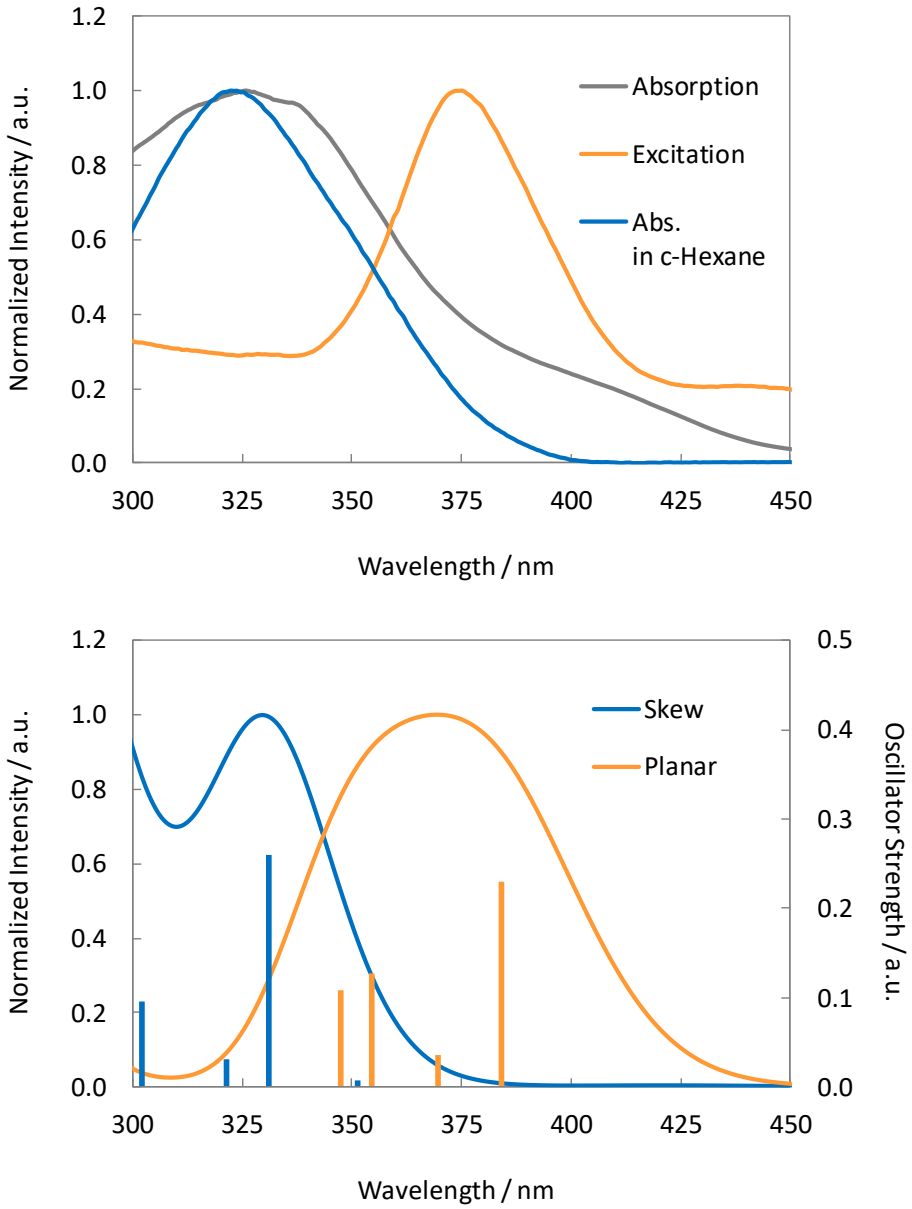

Figure S17. Top: the absorption spectrum of ground **BrH** (gray), excitation spectrum of ground **BrH** (orange, recorded at 610 nm), and absorption spectrum of **BrH** in cyclohexane (blue, 2.0×10^{-5} M). Bottom: simulated absorption spectra of the skew (blue) and planar (orange) conformers of **BrH** with the calculated oscillator strength.

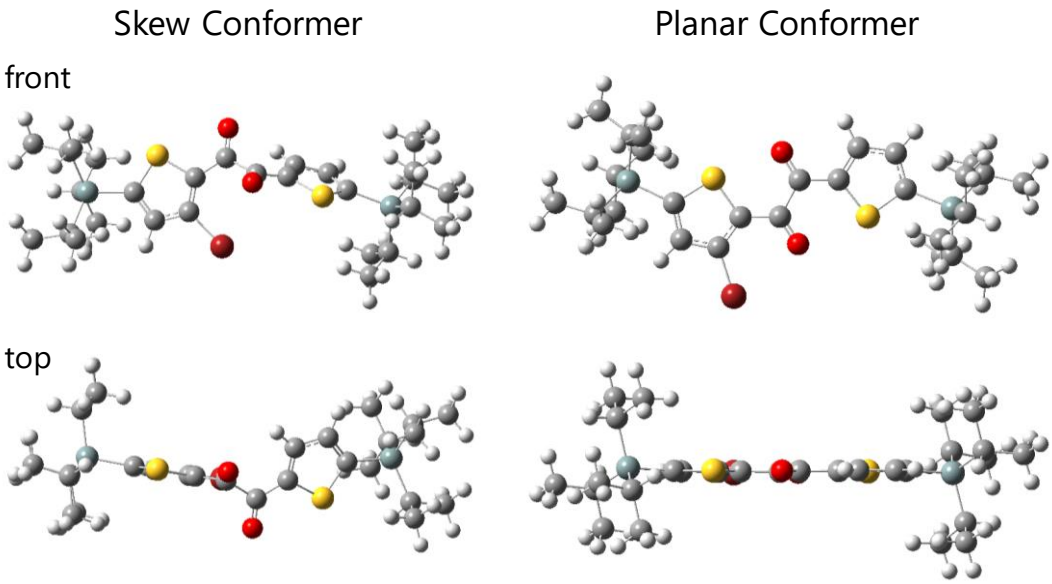

Figure S18. Optimized structures of **BrH** in the skew (left) and planar (right) conformations.

PL spectra of BrH in solution

Analytically pure **BrH** was dissolved in spectral-grade cyclohexane (4.0×10^{-5} M), and degassed by Ar bubbling for 8 min. The PL spectrum was obtained (λ_{ex} = 320 nm) using a JASCO FP-8200 spectrometer, which almost overlaps that of ground **BrH** powder (Figure S19), suggesting the conformational similarity of the emitting species. According to our previous study,[3] the skew conformer of **BrH** would relaxes to the planar conformer in solution, which is indeed common behavior of aromatic 1,2-diketones.[7] Therefore, we consider that the emissive conformer in solution and hence in the amorphous state would be the planar conformer.

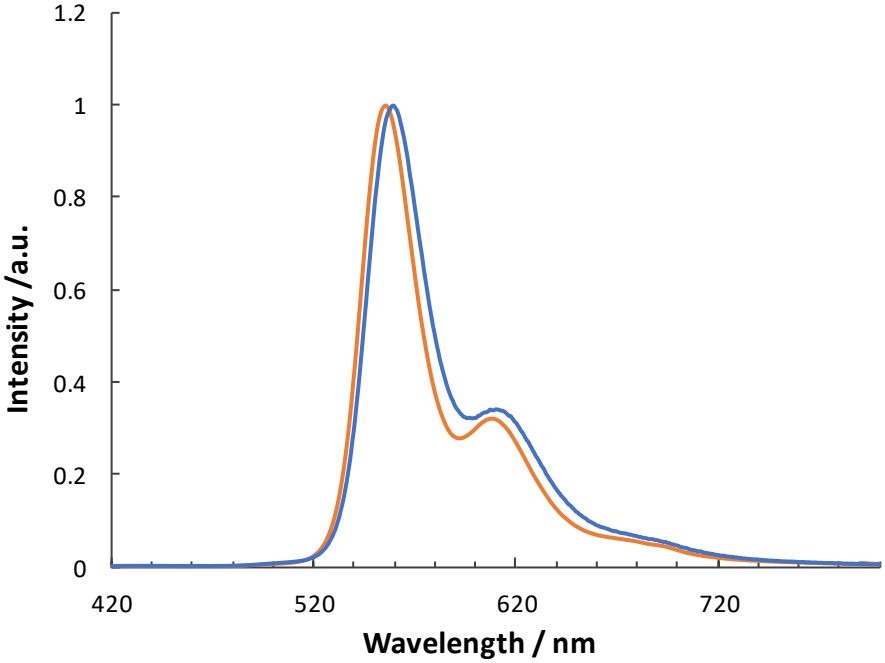

Figure S19. PL spectra of **BrH** in cyclohexane (orange, λ_{ex} = 320 nm) and ground solid (blue, λ_{ex} = 380 nm).

7. NMR Charts

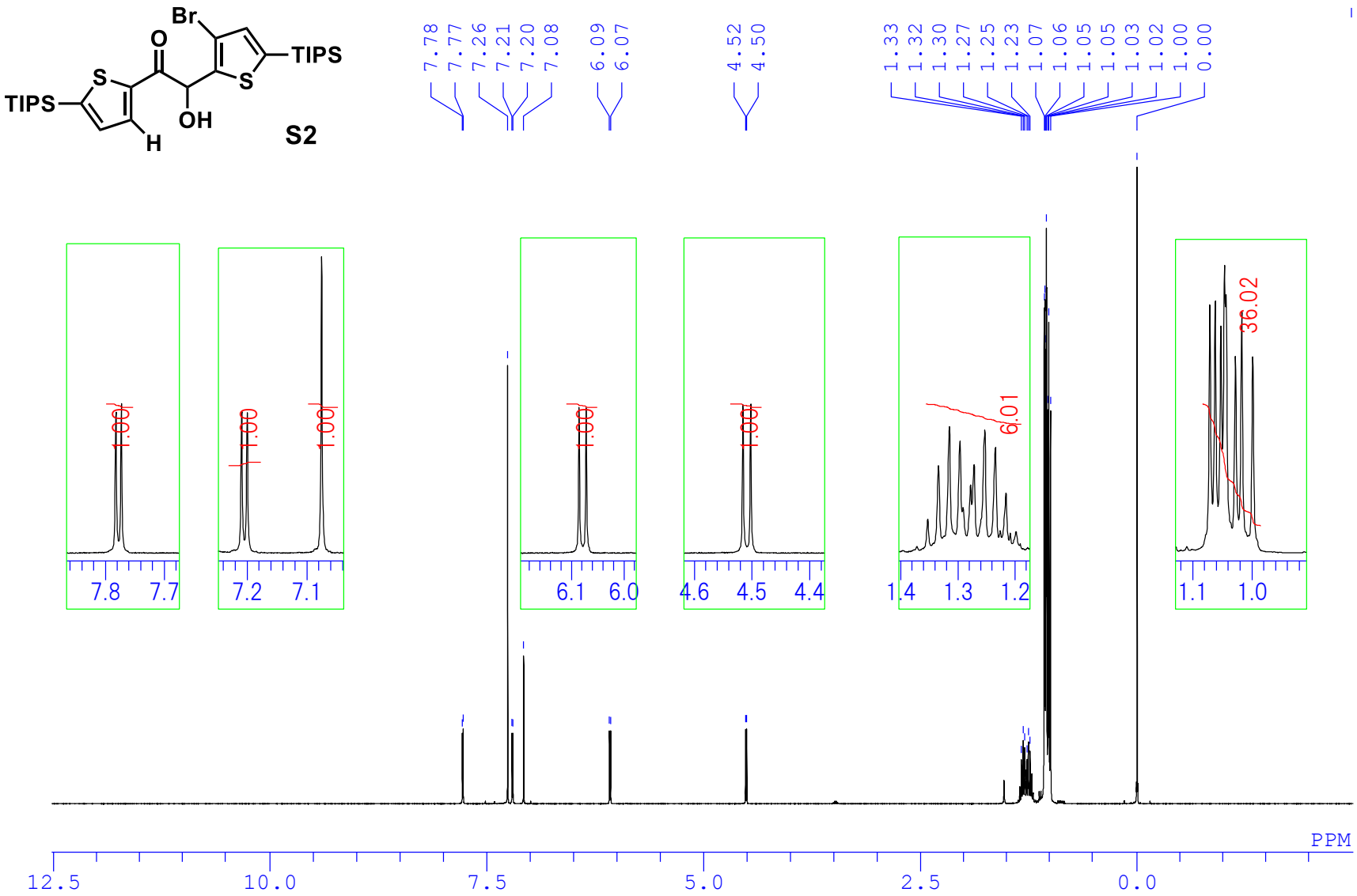
Br
O
TIPS
S
S
TIPS
OH
H
S2
7.78
7.77
7.26
7.21
7.20
7.08
6.09
6.07
4.52
4.50
1.33
1.32
1.30
1.27
1.25
1.23
1.07
1.06
1.05
1.05
1.03
1.02
1.00
0.00
1.00
1.00
1.00
1.00
1.00
6.01
36.02
7.8
7.7
7.2
7.1
6.1
6.0
4.6
4.5
4.4
1.4
1.3
1.2
1.1
1.0
PPM
12.5
10.0
7.5
5.0
2.5
0.0

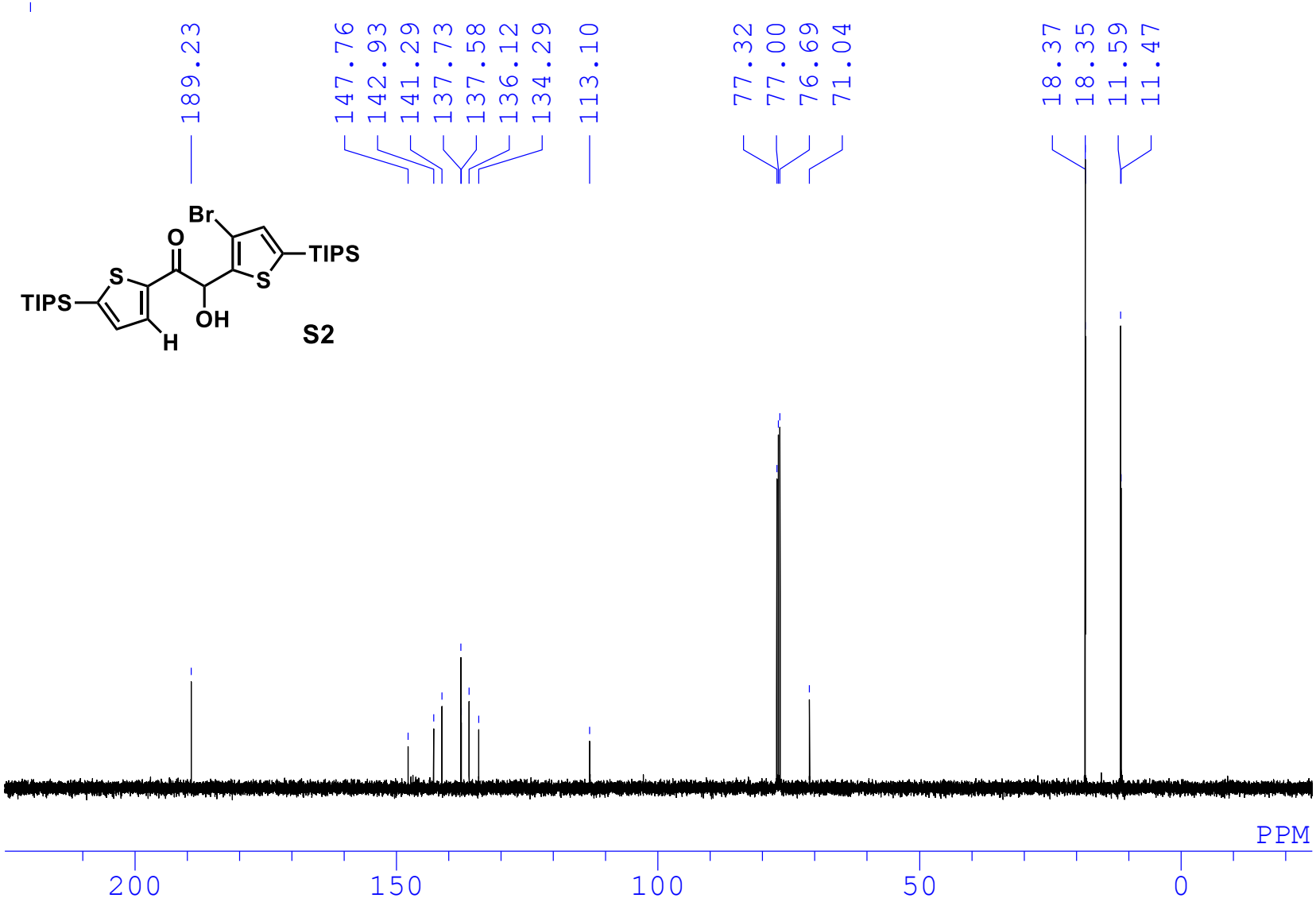
189.23
147.76
142.93
141.29
137.73
137.58
136.12
134.29
113.10
77.32
77.00
76.69
71.04
18.37
18.35
11.59
11.47
Br
O
TIPS
S
S
TIPS
OH
H
S2
PPM
200
150
100
50
0

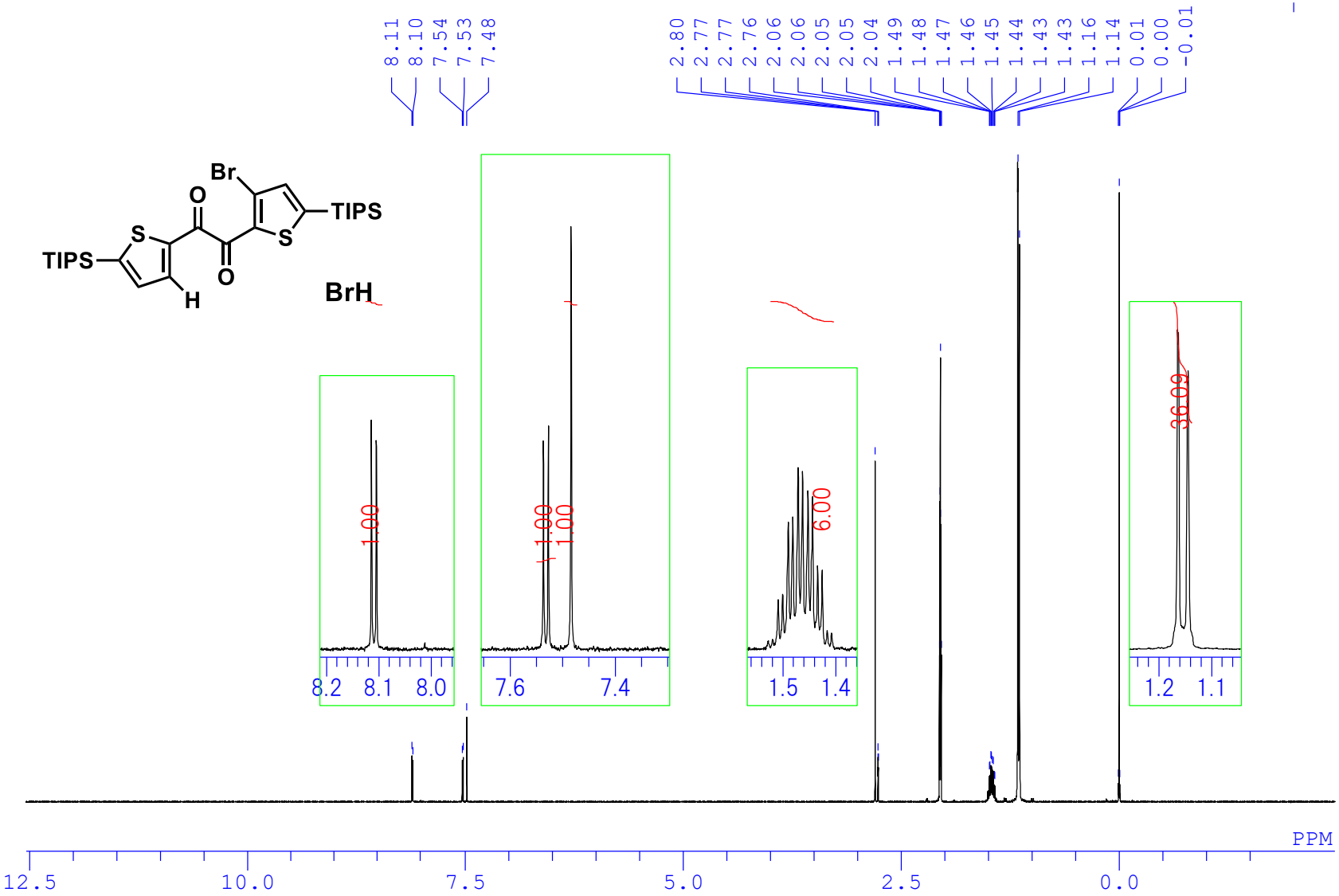
8.11
8.10
7.54
7.53
7.48
2.80
2.77
2.77
2.76
2.06
2.06
2.05
2.05
2.04
1.49
1.48
1.47
1.46
1.45
1.44
1.43
1.43
1.16
1.14
0.01
0.00
-0.01
Br
O
TIPS
S
S
TIPS
O
H
BrH
1.00
1.00
1.00
6.00
36.09
8.2
8.1
8.0
7.6
7.4
1.5
1.4
1.2
1.1
PPM
12.5
10.0
7.5
5.0
2.5
0.0

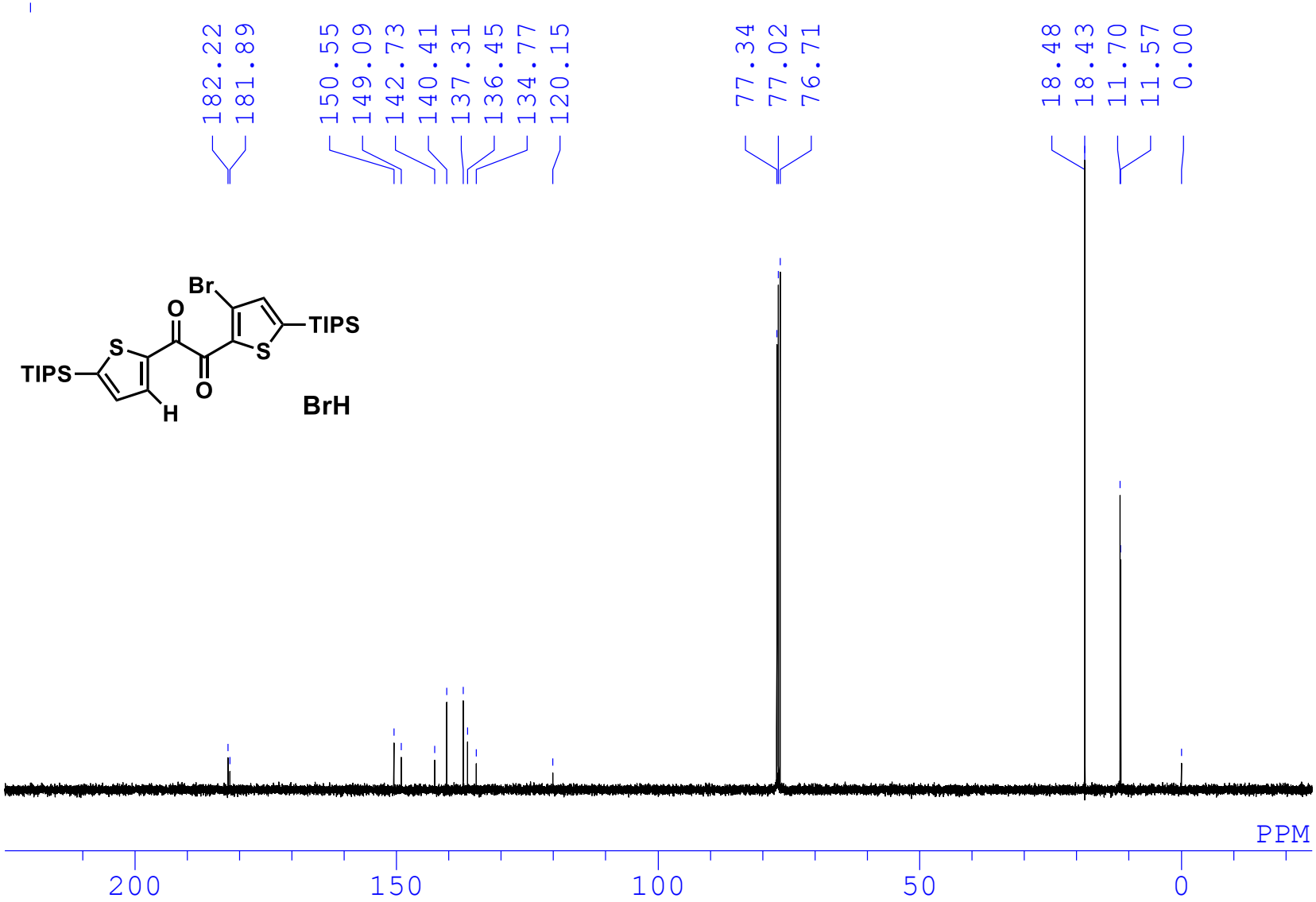
182.22
181.89
150.55
149.09
142.73
140.41
137.31
136.45
134.77
120.15
77.34
77.02
76.71
18.48
18.43
11.70
11.57
0.00
Br
O
TIPS
S
S
TIPS
O
H
BrH
PPM
200
150
100
50
0

8. References

1. (a) K. Suzuki, A. Kobayashi, S. Kaneko, K. Takehira, T. Yoshihara, H. Ishida, Y. Shiina, S. Oishi and S. Tobita, *Phys. Chem. Chem. Phys.*, 2009, **11**, 9850–9860; (b) A. M. Brouwer, *Pure Appl. Chem.*, 2011, **83**, 2213-2228.
2. A. B. Pangborn, M. A. Giardello, R. H. Grubbs, R. K. Rosen and F. J. Timmers, *Organometallics*, 1996, **15**, 1518-1520.
3. Y. Tani, M. Terasaki, M. Komura and T. Ogawa, *J. Mater. Chem. C*, 2019, **7**, 11926-11931.
4. E. G. Delany and S. J. Connon, *Org. Biomol. Chem.*, 2018, **16**, 780-786.
5. (a) A. Sakai, E. Ohta, Y. Matsui, S. Tsuzuki and H. Ikeda, *ChemPhysChem*, 2016, **17**, 4033-4036; (b) S. F. Boys and F. Bernardi, *Mol. Phys.*, 1970, **19**, 553-566.
6. M. J. Frisch, G. W. Trucks, H. B. Schlegel, G. E. Scuseria, M. A. Robb, J. R. Cheeseman, G. Scalmani, V. Barone, G. A. Petersson, H. Nakatsuji, X. Li, M. Caricato, A. V. Marenich, J. Bloino, B. G. Janesko, R. Gomperts, B. Mennucci, H. P. Hratchian, J. V. Ortiz, A. F. Izmaylov, J. L. Sonnenberg, Williams, F. Ding, F. Lipparini, F. Egidi, J. Goings, B. Peng, A. Petrone, T. Henderson, D. Ranasinghe, V. G. Zakrzewski, J. Gao, N. Rega, G. Zheng, W. Liang, M. Hada, M. Ehara, K. Toyota, R. Fukuda, J. Hasegawa, M. Ishida, T. Nakajima, Y. Honda, O. Kitao, H. Nakai, T. Vreven, K. Throssell, J. A. Montgomery Jr., J. E. Peralta, F. Ogliaro, M. J. Bearpark, J. J. Heyd, E. N. Brothers, K. N. Kudin, V. N. Staroverov, T. A. Keith, R. Kobayashi, J. Normand, K. Raghavachari, A. P. Rendell, J. C. Burant, S. S. Iyengar, J. Tomasi, M. Cossi, J. M. Millam, M. Klene, C. Adamo, R. Cammi, J. W. Ochterski, R. L. Martin, K. Morokuma, O. Farkas, J. B. Foresman and D. J. Fox, *Gaussian 16 Rev. B.01*, Wallingford, CT, 2016.
7. (a) D. S. Roy, K. Bhattacharyya, S. C. Bera and M. Chowdhury, *Chem. Phys. Lett.*, 1980, **69**, 134-140; (b) K. Bhattacharyya and M. Chowdhury, *J. Photochem.*, 1986, **33**, 61-65.